Improving optical bench radius measurements using stage error motion data

Tony L. Schmitz,[1] Neil Gardner,[2,3] Matthew Vaughn,[2]
Kate Medicus,[2,4] and Angela Davies[2,*]

[1]Department of Mechanical and Aerospace Engineering, University of Florida, Gainesville, Florida 32611, USA

[2]Department of Physics and Optical Science, University of North Carolina at Charlotte, Charlotte, North Carolina 28223, USA

[3]Now at ASML, Richmond, California 94806, USA

[4]Now at Mitutoyo Research Center, Netherlands

*Corresponding author: adavies@uncc.edu

Received 4 September 2008; accepted 23 September 2008;
posted 29 October 2008 (Doc. ID 101105); published 11 December 2008

We describe the application of a vector-based radius approach to optical bench radius measurements in the presence of imperfect stage motions. In this approach, the radius is defined using a vector equation and homogeneous transformation matrix formulism. This is in contrast to the typical technique, where the displacement between the confocal and cat's eye null positions alone is used to determine the test optic radius. An important aspect of the vector-based radius definition is the intrinsic correction for measurement biases, such as straightness errors in the stage motion and cosine misalignment between the stage and displacement gauge axis, which lead to an artificially small radius value if the traditional approach is employed. Measurement techniques and results are provided for the stage error motions, which are then combined with the setup geometry through the analysis to determine the radius of curvature for a spherical artifact. Comparisons are shown between the new vector-based radius calculation, traditional radius computation, and a low uncertainty mechanical measurement. Additionally, the measurement uncertainty for the vector-based approach is determined using Monte Carlo simulation and compared to experimental results.

OCIS codes: 220.4840, 120.3180, 120.3940, 120.6650.

1. Introduction

The radius is a primary descriptor of spherical and mildly aspherical optics. Accurate knowledge of this value is critically important when spacing individual elements in a lens assembly, for example. An optical bench is typically the preferred measurement platform to determine the radius with low uncertainty. On an optical bench, the radius is defined by the best-fit sphere over the clear aperture. It is determined using a phase measuring interferometer to identify two critical positions of the test optic: confocal and cat's eye. See Fig. 1, where the test optic is represented as a sphere without loss of generality. With the artifact at either of these positions, the wavefront reflects back on itself, and the interferometric cavity is null. A linear transducer measures displacement as the test optic is translated between the two null positions, and the recorded value is nominally the radius of the best-fit sphere to the surface. Although the test sequence is straightforward, there are a number of potential error sources. These include identification of null at confocal and cat's eye, wavefront aberrations in the interferometer, figure error of the measured surface, displacement transducer errors, and stage error motions between confocal and cat's eye, including both translational

0003-6935/08/366692-09$15.00/0

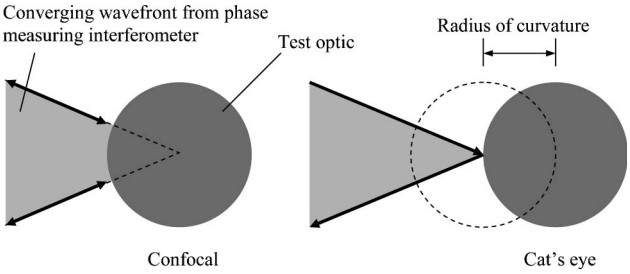

Fig. 1. Confocal and cat's eye interferometric null positions for optical bench radius measurements. In the absence of all errors, the displacement between these two positions gives the test optic radius of curvature over the clear aperture of the phase measuring interferometer.

and rotational deviations from the nominally single degree of freedom motion along the transducer axis [1–7].

The importance of considering the stage error motions is demonstrated in Fig. 2. An example is translation error in the y direction during the z direction motion between confocal and cat's eye results in a transducer value that is less than the radius by the sag in the surface. Note that the transducer reading is less than the true radius regardless of the error sign; this leads to a bias in the radius measurement. In subsequent sections, this translation error will be referred to as a straightness error of the z motion in the y direction and is designated as $\delta_y(z)$. By this notation, it is emphasized that the error is a (nonlinear) function of the z position, in general. Other error motions include straightness error of the z motion in the x direction, $\delta_x(z)$, and rotational errors about the x, y, and z axes during z motion, $\varepsilon_x(z)$, $\varepsilon_y(z)$, and $\varepsilon_z(z)$, respectively. The rotational errors couple with offsets between the transducer axis and interferometer optical axis to produce the well known Abbe errors.

The purpose of this paper is to demonstrate improved radius measurement accuracy on a typical optical bench using (1) the vector definition of radius described in Refs. [8–10], (2) measurements of the stage error motions, and (3) measurements of geometric offsets that depend on the optical bench configuration. The following sections describe the vector definition of the radius measurement, error motion measurements, and the final measurement results for a calibrated (24.5 mm radius) Zerodur sphere. The results show that using a commercial instrument and the traditional radius measurement, the measured radius of the calibrated sphere is 35 μm too small. This bias is removed when we apply our vector-based error motion correction. The primary benefit of this approach is that it is no longer necessary to engineer a high quality optical bench to realize accurate measurements. Rather, the error motions must simply be repeatable and well characterized because our approach directly compensates for their influence.

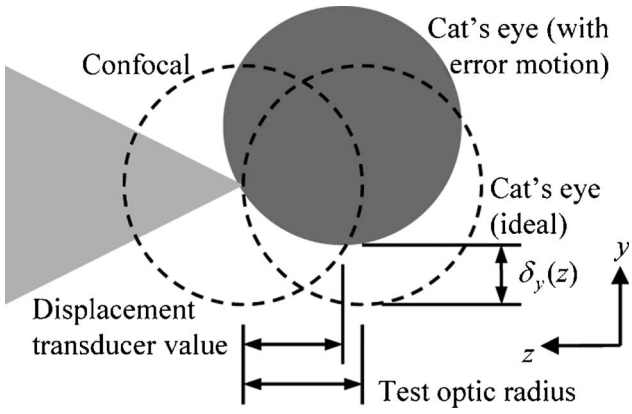

Fig. 2. In the presence of stage error motions, depicted simply as a y straightness error in the z motion here, a biased radius value is obtained from the linear transducer displacement.

2. Vector Radius Definition

Our vector-based approach, which compensates for errors in the stage motion between confocal and cat's eye, is applied to define the radius, R, in Ref. [10]. The method is based on a homogeneous transformation matrix (HTM) formalism and intrinsically leads to an unbiased estimate of R. The method defines the radius as the magnitude of the difference between two vectors rather than a simple projection onto the displacement transducer axis, as seen in Fig. 2. One of the vectors captures the stage, and therefore the test optic motion, and the other defines the focus location of the wavefront exiting the interferometer. This focus location can be thought of as the "probe" used to identify the optic center of curvature (confocal) and surface (cat's eye). The HTM approach [11–13] is well known in the precision engineering community and is commonly used to compensate error motions in machining centers and coordinate measuring machines.

A vector relationship describing R requires the definition of two coordinate frames. The first is attached to the stage that carries the test optic. The second, our reference coordinate frame, is fixed to ground and is used to locate the probe (interferometer focus). The reference z axis is taken to be coincident with the displacement transducer axis. The two frames are identified in Fig. 3. The test optic is rigidly attached to the stage and is therefore fixed in the stage coordinate frame. Its center of curvature is located by the vector, ${}^s\vec{X}_t$, where the subscript indicates the test optic (t) and the superscript the stage (s) coordinate frame. The probe (p) location is identified by a vector expressed in reference (r) frame coordinates, ${}^r\vec{X}_p$. These two vectors are also shown in Fig. 3.

A radius measurement is depicted in Fig. 4. The reference and stage coordinate frames are initially coincident at the confocal position (panel a). The stage and test optic are then moved to the cat's eye position (panel b). In the example shown, the $\delta_y(z)$ error motion causes the displacement transducer value, measured along the stage z axis, to be less than the actual radius, described by the vector $\vec{R}$ in Fig. 4.

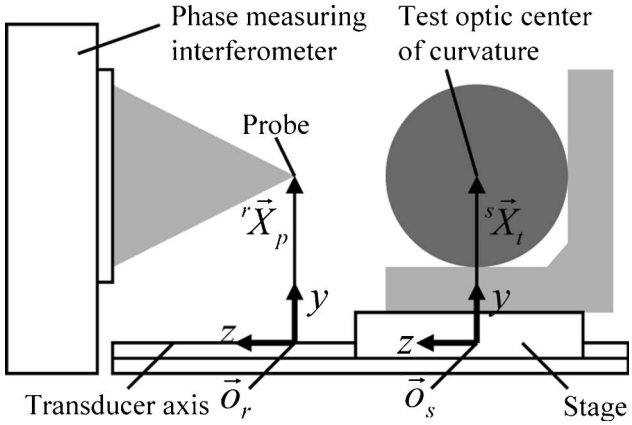

Fig. 3. Coordinate frames for vector radius definition. The reference frame is fixed and has the origin $\vec{o}_r$. The stage frame with origin $\vec{o}_s$ is attached to the moving stage, which carries the test optic.

The new vector definition of radius is shown in Fig. 5. Here a new vector, ${}^r\vec{X}_t^{\mathrm{ce}}$, is introduced that identifies the test optic center of curvature in the reference frame, rather than the stage frame. The trailing superscript, ce, emphasizes that this vector is defined when the test optic is in the cat's eye position. This enables construction of the vector equation ${}^r\vec{X}_t^{\mathrm{ce}} + \vec{R} = {}^r\vec{X}_p$. Solving for $\vec{R}$ gives $\vec{R} = {}^r\vec{X}_p - {}^r\vec{X}_t^{\mathrm{ce}}$, the magnitude of which is the quantity of interest. Unfortunately, ${}^r\vec{X}_t^{\mathrm{ce}}$ is not explicitly known. It is determined by the position of the test optic in the stage frame and the detailed motion of the stage during the translation from confocal to cat's eye. An HTM can be used to transform the coordinates and to take this motion into account. An HTM is a 4×4 matrix that captures the (small) rotations and/or translations of one coordinate system relative to another, and enables a vector described in one system to be mapped to the other [11–13]. Equation (1) shows the HTM, ${}^rT_s$, for this case:

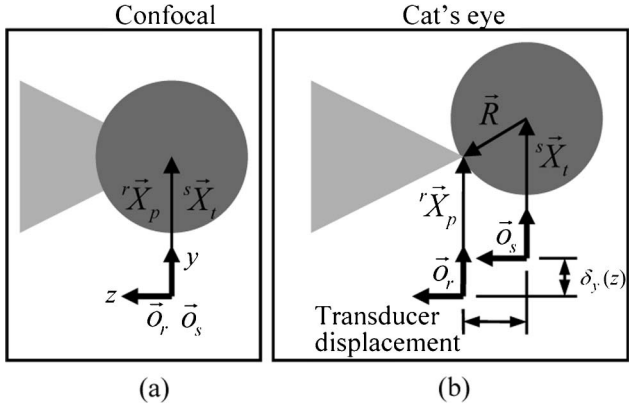

Fig. 4. Illustration of radius measurement on an optical bench. The reference and stage coordinate frames are identified for the (a) confocal and (b) cat's eye positions.

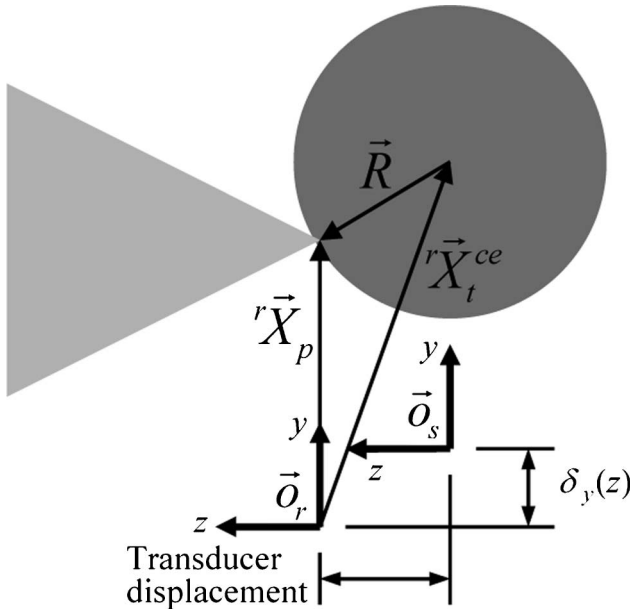

Fig. 5. Vector-based radius definition. The radius is not defined by the linear transducer value only, but by the vector equation ${}^r\vec{X}_t^{ce} + \vec{R} = {}^r\vec{X}_p$.

$$ {}^rT_s = \begin{bmatrix} 1 & -\varepsilon_z(z) & \varepsilon_y(z) & \delta_x(z) \\ \varepsilon_z(z) & 1 & -\varepsilon_x(z) & \delta_y(z) \\ -\varepsilon_y(z) & \varepsilon_x(z) & 1 & d \\ 0 & 0 & 0 & 1 \end{bmatrix}, \qquad (1) $$

where d is the displacement recorded by the linear transducer during the z motion between confocal and cat's eye, the error motions are the parasitic displacements and rotations that occurred between confocal and cat's eye, and the "1" in the (4,4) position indicates unity scaling. Using Eq. (1), ${}^r\vec{X}_t^{\mathrm{ce}}$ is determined from ${}^r\vec{X}_t^{\mathrm{ce}} = {}^rT_s\,{}^s\vec{X}_t$. The test optic radius is defined as the magnitude of $\vec{R}$, so the final radius expression is

$$ R^2 = |\vec{R}|^2 = |{}^r\vec{X}_p - {}^r\vec{X}_t^{\mathrm{ce}}|^2 = |{}^r\vec{X}_p - {}^rT_s\,{}^s\vec{X}_t|^2. \qquad (2) $$

Because the reference and stage frames are coincident at the confocal position (Fig. 4), ${}^s\vec{X}_t$ can be written as

$$ {}^s\vec{X}_t = {}^r\vec{X}_p + \begin{bmatrix} dx^{\mathrm{cf}} \\ dy^{\mathrm{cf}} \\ dz^{\mathrm{cf}} \\ 1 \end{bmatrix} = \begin{bmatrix} {}^rx_p + dx^{\mathrm{cf}} \\ {}^ry_p + dy^{\mathrm{cf}} \\ dz^{\mathrm{cf}} \\ 1 \end{bmatrix}, \qquad (3) $$

where dx_{cf}, dy_{cf}, and dz_{cf} represent errors in the capability to null the interferometer at confocal in the three coordinate directions, it is assumed that the z direction offset of the probe in the reference coordinate system is zero, and the "1" entry in the (4,1) position is a placeholder to provide dimensional compatibility with the 4×4 HTM, ${}^rT_s$. Inserting Eqs. (1) and (3) in Eq. (2) gives the full expression for the radius. See Eq. (4). Expanding Eq. (4) gives

Eq. (5). The estimate of the radius is then equal to the square root of Eq. (5), i.e., $R = \sqrt{\langle R^2 \rangle}$, where the angled bracket represents the expectation value. The expectation, or expected, value is mathematically defined as the product of the parameter and its probability distribution integrated over all possible values [14]. All parameters are assumed to be uncorrelated:

$$R^2 = |\vec{R}|^2 = \left| \begin{bmatrix} {}^r x_p \\ {}^r y_p \\ 0 \\ 1 \end{bmatrix} - \begin{bmatrix} 1 & -\varepsilon_z(z) & \varepsilon_y(z) & \delta_x(z) \\ \varepsilon_z(z) & 1 & -\varepsilon_x(z) & \delta_y(z) \\ -\varepsilon_y(z) & \varepsilon_x(z) & 1 & d \\ 0 & 0 & 0 & 1 \end{bmatrix} \begin{bmatrix} {}^r x_p + dx^{\mathrm{cf}} \\ {}^r y_p + dy^{\mathrm{cf}} \\ dz^{\mathrm{cf}} \\ 1 \end{bmatrix} \right|^2, \tag{4}$$

$$\begin{aligned} R^2 = {} & [-dx^{\mathrm{cf}} + \varepsilon_z(z)({}^r y_p + dy^{\mathrm{cf}}) - \varepsilon_y(z) dz^{\mathrm{cf}} - \delta_x(z)]^2 \\ & + [-dy^{\mathrm{cf}} - \varepsilon_z(z)({}^r x_p + dx^{\mathrm{cf}}) + \varepsilon_x(z) dz^{\mathrm{cf}} - \delta_y(z)]^2 \\ & + [-dz^{\mathrm{cf}} + \varepsilon_y(z)({}^r x_p + dx^{\mathrm{cf}}) \\ & - \varepsilon_x(z)({}^r y_p + dy^{\mathrm{cf}}) - d]^2. \end{aligned} \tag{5}$$

Once the error motions are characterized, if repeatable, the values may be simply substituted into Eq. (5) to arrive at our improved estimate of the radius.

3. Measurement of Error Motions

The optical bench selected for this study is a 100 mm aperture phase measuring interferometer (Veeco RTI 4100) with a linear slide (THK Y3V008) and digital encoder (Renishaw, 0.25 μm resolution) oriented nominally parallel to the motion axis and the interferometer's horizontal optical axis. See Fig. 6. Measurements of the rotational and translational errors during z motion from confocal to cat's eye for this system are detailed in the following paragraphs. It is important that the error motions be measured relative to the reference (displacement transducer) axis. We measure the error motions over a motion range just beyond the confocal and cat's eye positions; then only the change in the angle and/or translation errors between the confocal and cat's eye positions are used for Eq. (5).

A. Rotational Error Motions

The rotational errors were measured using two different setups. First, $\varepsilon_x(z)$ (pitch) and $\varepsilon_y(z)$ (yaw) were measured using the phase measuring interferometer directly. A transmission flat was mounted to the interferometer to give a planar wavefront, and a return flat was mounted to the stage to provide a target. See Fig. 7. The fringe pattern was nulled, and the stage location was then incremented in z steps of 0.85 mm (~0.033 in) from the approximate confocal to cat's eye positions. At each step, the z position was recorded using the slide's digital encoder. The tilt coefficients due to the slide's rotational errors were determined using phase shifting to find the optical path difference map between the transmission and return flats. The tilt coefficients were then used to compute $\varepsilon_x(z)$ and $\varepsilon_y(z)$. To determine the repeatability, ten measurement sets were completed over the 25.4 mm range (the radius test optic was a calibrated Zerodur sphere with a radius of approximately 24.5 mm so the 25.4 mm range was sufficient). The average rotational error and standard deviation, σ, for the ten sets at each measurement location are provided in Fig. 8. A range of 152.6 μrad with an average σ of 6.2 μrad is observed for $\varepsilon_x(z)$, while a range of 93.2 μrad with an average σ of 3.8 μrad is observed for $\varepsilon_y(z)$. In both cases, the trends are approximately linear, but this cannot be assumed in general. In Fig. 8 confocal was located near $z = 0$ and cat's eye near $z = -24.5$ mm. Note that this sign convention matches Fig. 5 and the rotational errors obey the right hand rule, as pictured.

The rotational error $\varepsilon_z(z)$ (referred to as roll) was measured using a differential electronic level consisting of two sensing heads (electronic levels, Federal EGH-13W1) and a single amplifier (Federal EAS-

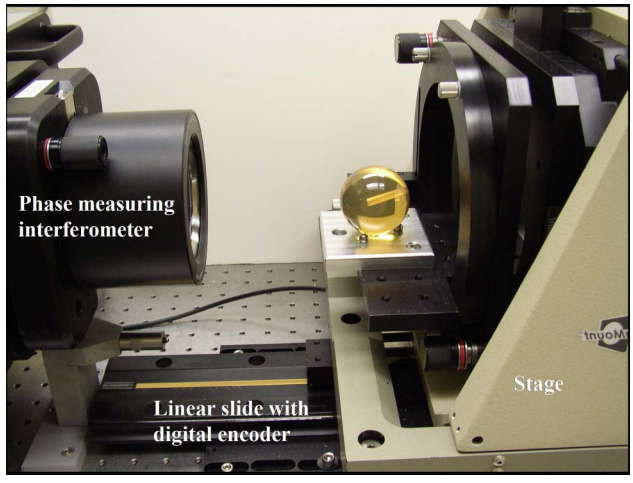

Fig. 6. (Color online) Photograph of the optical bench. The linear slide and stage are used to position the test optic relative to the probe (the phase measuring interferometer converging wavefront focus—not visible). The displacement is recorded using the digital encoder attached to the slide.

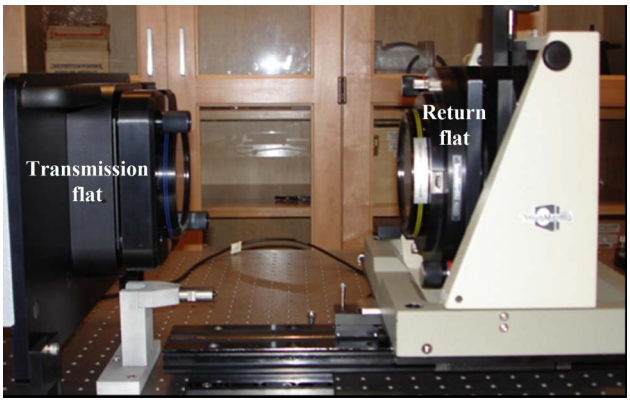

Fig. 7. (Color online) Setup for rotational error measurements. The tilt coefficients from the interferometric phase maps were used to calculate $\varepsilon_x(z)$ and $\varepsilon_y(z)$.

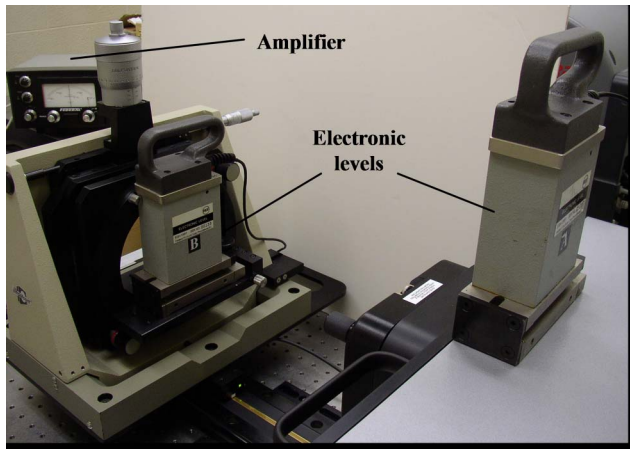

Fig. 9. (Color online) Setup for the $\varepsilon_z(z)$ measurements.

2150). One electronic level was attached to the stage, and the other was mounted to the interferometer to provide a fixed reference. Differences in rotation about the z axis between the two levels were amplified and recorded every 1.68 mm (0.066 in.) over the same 25.4 mm z range. The setup is shown in Fig. 9 and the results are provided in Fig. 10. A total of ten repetitions were again completed and the standard deviation error bars are included. The range is 46.1 μrad and the average σ is 3.4 μrad.

B. Straightness Error Motions

The straightness error motions in the x and y directions for the z motion contribute to the terms, $\delta_x(z)$ and $\delta_y(z)$. A fixed angle misalignment between the motion axis and the displacement transducer axis (referred to as squareness) also contributes to these terms. The squareness error is nominally zero in this instrument; therefore we need only measure the straightness error for our estimates of $\delta_x(z)$ and $\delta_y(z)$. Uncertainty in our squareness condition is considered in the uncertainty analysis, however. The straightness error motions were collected using a dial indicator and reference surface (straightedge). To avoid the requirement for a highly accurate and costly straightedge, a nominally flat steel block was used, and the well known straightedge reversal technique was applied [15]. (Because the test optic size was small in this case, a 24.5 mm diameter sphere, an optical flat would also have provided an acceptable reference surface.) In this approach, the dial indicator is used to sample lateral deviations relative to the straightedge in two orientations in order to distinguish between slide error motions and imperfections in the straightedge. The first setup is described by Eq. (6), where $M(z)$ is the slide (or machine) straightness as a function of the z position, $S(z)$ is the straightedge flatness deviations, and $I_1(z)$ represents the indicator values. See Fig. 11. In the second setup, the block is elevated and turned upside down and the indicator orientation is reversed to again measure the same block surface, but from the opposite direction. This causes the relative contribution of the slide error to switch sign as shown in Eq. (7). The slide straightness is then computed as shown in Eq. (8). The setup-dependent slope of $M(z)$ is finally removed to isolate the straightness error. Note that the straightness measurement must be performed as coincident as possible with the displacement transducer axis.

$$I_1(z) = M(z) + S(z), \tag{6}$$

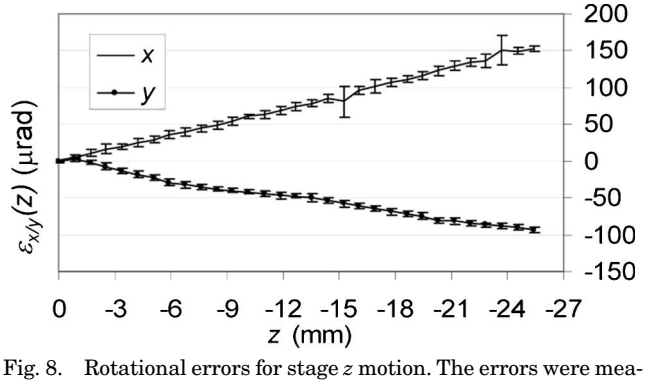

Fig. 8. Rotational errors for stage z motion. The errors were measured using a transmission/return flat setup on the phase measuring interferometer. The mean values and standard deviations from ten repeated tests are shown.

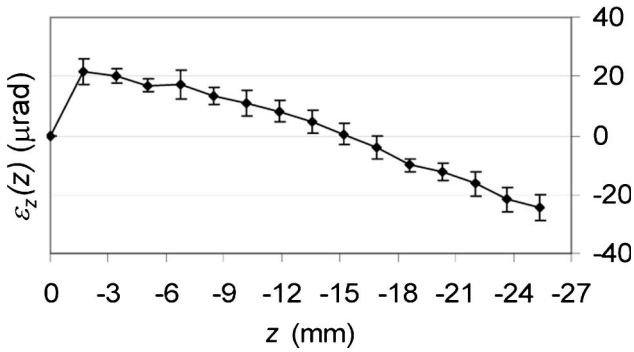

Fig. 10. Measurements results for $\varepsilon_z(z)$. The data were collected using an electronic level system.

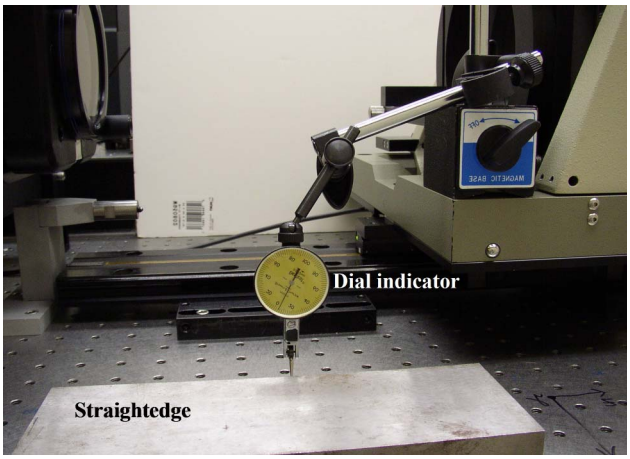

Fig. 11. (Color online) First setup for y straightness of z motion, $\delta_y(z)$, measurement.

$$I_2(z) = -M(z) + S(z), \tag{7}$$

$$M(z) = \frac{I_1(z) - I_2(z)}{2}. \tag{8}$$

The measurements results are displayed in Figs. 12 and 13 for the x and y directions, respectively. A total of ten repetitions were completed, and the standard deviation error bars are included.

C. Offsets

In addition to the error motions, the offsets between the reference coordinate frame origin and probe location in the x and y directions, ${}^{r}x_p$ and ${}^{r}y_p$, are also required. See Fig. 5 and Eq. (5). As shown in Fig. 14, the reference frame was fixed at the surface of the digital encoder at the nominal z location of the probe. The vertical offset, ${}^{r}y_p$, was determined to be 166 mm using a height gauge that was zeroed at the encoder surface and raised to the converging wavefront focus. The horizontal offset, ${}^{r}x_p$, was visually estimated at 13 mm. Again, these values follow the coordinate system sign convention.

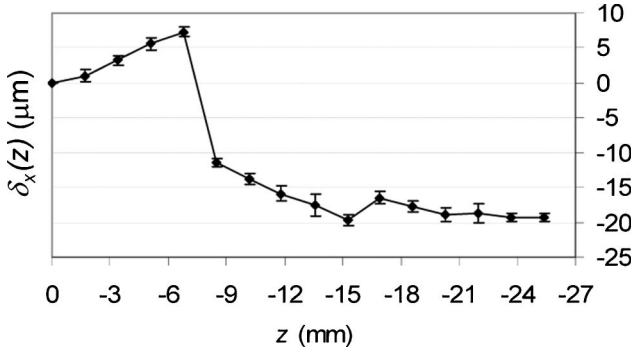

Fig. 12. Straightness errors in the x direction for z motion, $\delta_x(z)$.

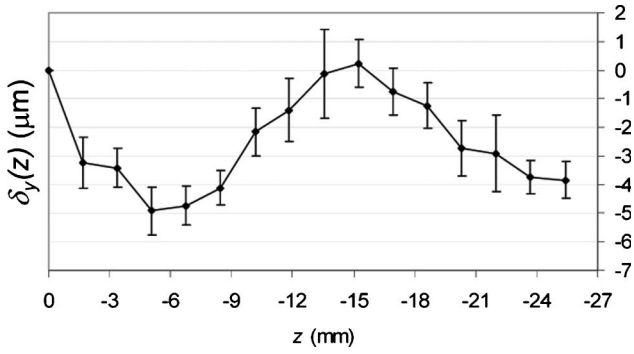

Fig. 13. Straightness errors in the y direction for z motion, $\delta_y(z)$.

4. Results

Radius measurements were completed using a Fizeau configuration of the phase measuring interferometer with an $f/1.5$ transmission sphere (Optimax, 100 mm aperture). The test artifact was a 24.466 mm radius Zerodur sphere. The radius was calibrated on a Moore-48 coordinate measuring machine (CMM) at the National Institute of Standards and Technology, Gaithersburg, Maryland, USA. The combined standard uncertainty, u_c, for the calibration is 50 nm. The null locations and corresponding linear encoder values for the interferometric radius measurements were determined by three procedures: (1) visual examination of null interference fringes, (2) correction for nonnull conditions using the interferometer manufacturer's software algorithm, and (3) a linear regression to the Zernike a_2^0 (power) coefficients obtained from optical phase difference maps at a series of z positions near confocal and cat's eye. For the latter, the measurement procedure is demonstrated in Fig. 15.

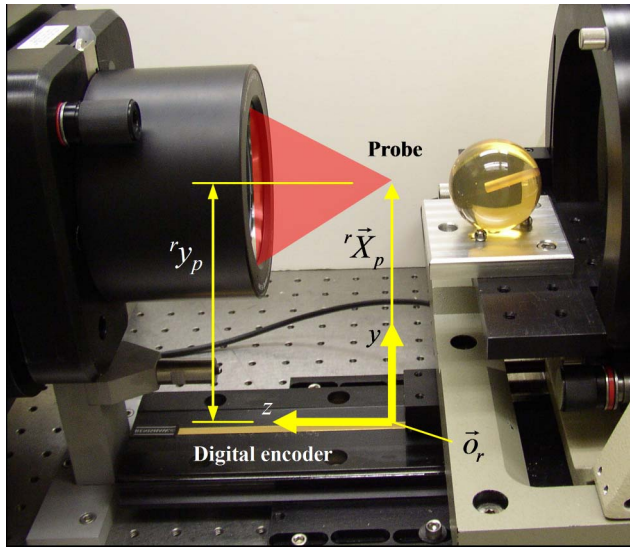

Fig. 14. (Color online) Illustration of probe location in reference coordinate frame.

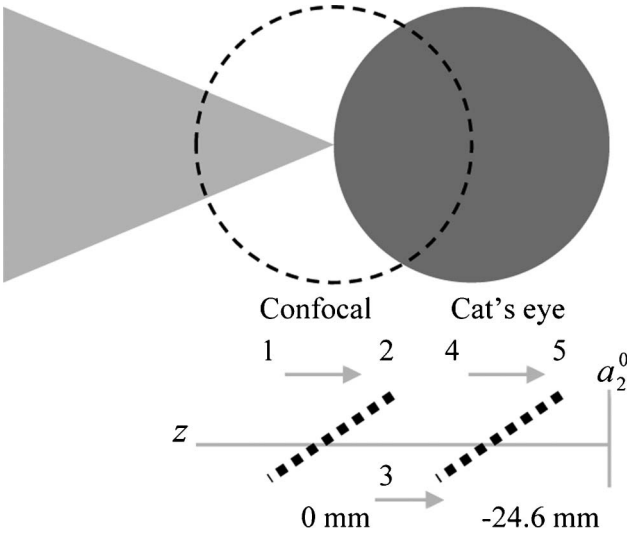

Fig. 15. Measurement sequence for determining confocal and cat's eye locations by linear regression. A sequence of phase maps is recorded at z positions on each side of confocal (1 to 2) and cat's eye (4 to 5). The best fit line is used to determine the null location. The 3 to 4 step is translation between confocal and cat's eye. Note that the z direction is positive to the left.

A. Monte Carlo Simulation

In the traditional radius measurement, the radius would be determined by the displacements obtained from the linear encoder alone. However, we show that Eq. (5) must be applied in the presence of stage error motions to obtain an unbiased radius estimate. There is uncertainty in the terms contributing to Eq. (5) and this affects the radius uncertainty. With such a complicated nonlinear equation for the measurand, a Monte Carlo simulation is the ideal approach to determine both the mean (expected) radius value and the associated standard deviation (combined standard uncertainty). The Monte Carlo simulation was selected because direct substitution of the input mean values into the measurand (or quantity under test) equation is correct only if the equation is a linear combination of the random variables and Eq. (5) is clearly nonlinear [14]. Rigorously, the expectation value of an arbitrary function is equal to the function (e.g., Eq. (5)) multiplied by the probability distributions for all random variables integrated over all possible values of the random variables (assuming the random variables are uncorrelated) [14]. Only if the function is linear does this simplify and equate to a direct substitution of expectation values.

The Monte Carlo simulation proceeded by randomly selecting a value for each input variable (dx^{cf}, dy^{cf}, dz^{cf}, ${}^{r}x_p$, ${}^{r}y_p$, d, $\delta_x(z)$, $\delta_y(z)$, $\varepsilon_x(z)$, $\varepsilon_y(z)$, and $\varepsilon_z(z)$) from the specified distribution, calculating R, and repeating these steps over many iterations (1×10^5). The mean value and standard deviation (or standard uncertainty) for each input are described in the following paragraphs. Normal distributions were assumed unless otherwise specified, and the variables were assumed to be uncorrelated.

The confocal nulling uncertainties were estimated based on a residual 0.2 wave fringe pattern in the "nulled" condition. The dz^{cf} uncertainty was set equal to the 0.2 wave error divided by the average slope of the a_2^0 versus z line from multiple confocal null linear regressions (~46 waves/mm). The resulting 4 μm standard uncertainty was used for dx^{cf}, dy^{cf}, and dz^{cf}. Zero mean values were assumed.

As noted, ${}^{r}y_p$ was estimated to be 166 mm using a height gauge. The standard uncertainty was set to 0.13 mm based on the manufacturer's recommendation. The mean value of ${}^{r}x_p$ was 13 mm; the standard uncertainty in the visual estimation technique was selected to be 1 mm.

The displacement recorded by the linear encoder between confocal and cat's eye, d, was 24.431 mm. This value was the average of multiple measurements using the linear regression procedure for null identification. The standard uncertainty of 0.7 μm was set by the standard deviation in d from the same measurement set (eight repetitions with eight points each at confocal and cat's eye).

The value of the error motions at the confocal and cat's eye positions were determined by linear interpolation between the individual measurement points identified in Figs. 8, 10, 12, and 13. The mean null locations were obtained from the same data set used to identify d. The standard uncertainty in the rotational error motions was conservatively set equal to the maximum standard deviation recorded at any point over the multiple repetitions. For the translational errors, the uncertainty from a potential cosine misalignment between the linear encoder axis and slide axis was considered. Based on a maximum misalignment of 1 deg, or $\frac{\pi}{180}$ rad, the standard uncertainties, u, for $\delta_x(z)$ and $\delta_y(z)$ were calculated using Eq. (9), where the $\sqrt{3}$ factor indicates a uniform distribution of the misalignment angle and a probability of 100% that the actual value lies within the ± 1 deg range [16]:

$$u = \frac{\frac{\pi}{180}}{\sqrt{3}} d. \tag{9}$$

Example Monte Carlo results are displayed in Fig. 16. The mean radius is 24.459 mm, and the standard deviation (combined standard uncertainty) is 7 μm. The mean value represents a bias correction of 28 μm relative to the linear encoder value of 24.431 mm. Figure 17 shows the comparison between the traditional radius approach and our vector-based approach. We also compare the three null identification methods. All of these values can be compared to the calibrated value for the sphere, which is also shown in the figure. The Monte Carlo result includes error bars that represent a coverage factor of $k = 2$ (~95% confidence interval) to arrive at an expanded uncertainty, U, of 14 μm.

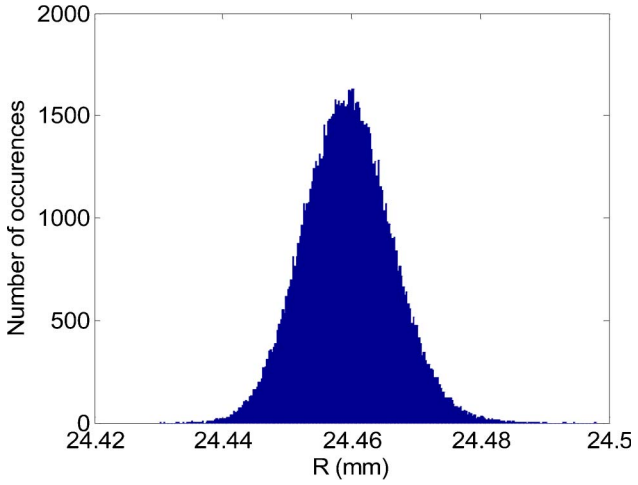

Fig. 16. (Color online) Monte Carlo simulations results for unbiased radius estimate using the vector-based definition.

5. Discussion

The data points identified by the open circles (visual null identification), triangles (software null correction), and diamonds (linear regression) in Fig. 17 represent the traditional radius measurement results and show an average 35 μm bias with respect to the calibrated (CMM) value. Careful identification of the null using a linear regression approach or the software null correction provides more repeatable radius estimates, but the result is still biased. The standard deviations (repeatability) corresponding to the three null identification approaches are 11 μm, 1 μm, and 0.7 μm, respectively. The vector-based radius definition (identified by the square) clearly yields a more accurate radius estimate. With a 95% confidence interval, the vector-based approach shows a corrected measurement bias in agreement with the calibrated value.

By isolating single error motion terms in the Monte Carlo simulation, we can explore the dominant cause of the bias correction. For this instrument, we find that the bias in the traditional radius measurement is dominated by two factors, an Abbe error and the uncertainty in the cosine error. The Abbe error is caused by the combination of the Abbe offset, ${}^{r}y_p$, and the rotational error motions. As pointed out in the literature [6], the uncertainty in the cosine error *alone* surprisingly leads to a bias in the measurement. Also, the bias is quite sensitive to the uncertainty level in the misalignment between the motion and linear encoder axes (note that this uncertainty indicates a lack of knowledge regarding the squareness between the two axes). The sensitivity is shown in Fig. 18, which summarizes Monte Carlo results for a range of possible cosine error uncertainties. The expected cosine error is still taken to be zero. Only the uncertainty is increased and varies between 0 and ±2 deg (recall that a ±1 deg uncertainty range was assumed for the result shown in Fig. 17). All other inputs were identical to the values previously described. We see that the mean value of R is quite sensitive to the possible misalignment and an uncertainty range between ±1.8 deg and ±1.9 deg completely removes the bias between the interferometric and mechanical Zerodur sphere measurements. The error bars in this figure are based only on the standard deviation obtained from the Monte Carlo simulation. No coverage factor was applied.

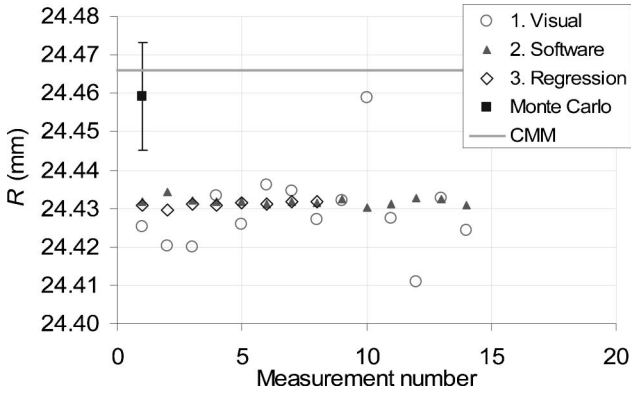

Fig. 17. Summary of Zerodur sphere radius measurements results.

6. Conclusions

This paper described a case study for identifying an unbiased radius estimate and associated uncertainty using a vector-based radius definition and a Monte Carlo simulation. Unlike the traditional optical bench approach that relies solely on the recorded displacement between the confocal and cat's eye null positions, radius was defined here using a vector equation and homogeneous transformation matrix formulism. The vector-based approach enabled the stage error motions to be considered directly in the radius calculation. Experimental results and measurement techniques were provided for the stage error motions, which were then combined with the setup geometry, to determine the unbiased radius estimate and combined standard uncertainty for a spherical artifact. Comparisons between the

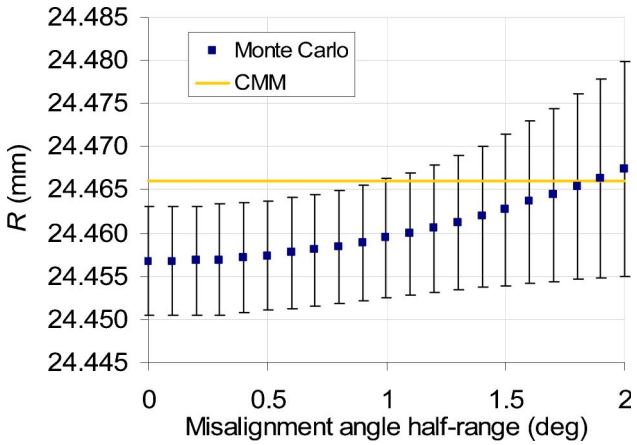

Fig. 18. (Color online) Sensitivity of mean radius value to uncertainty in the alignment angle between the stage and interferometer axes.

vector-based radius calculation, traditional radius computations, and a mechanically calibrated value show that the vector-based definition provides an accurate radius of curvature estimate. The important outcome is that, provided the error motions are well characterized and repeatable, accurate radius measurements can be performed on a less expensive optical bench when using the radius-based definition to calculate the radius of curvature.

This material is based upon work supported by the National Science Foundation (NSF) under grants 0348142 and 0555645. Any opinions, findings, and conclusions or recommendations expressed in this material are those of the authors and do not necessarily reflect the views of the National Science Foundation. The authors also wish to thank U. Griesmann, National Institute of Standards and Technology, for the use of the Zerodur sphere and T. Doiron and J. Stoup, National Institute of Standards and Technology, for performing the mechanical measurements of the Zerodur sphere.

References

1. D. Malacara, *Optical Shop Testing* (Wiley, 1992).
2. M. Murty and R. Shukla, "Measurements of long radius of curvature," Opt. Eng. **22**, 231–235 (1983).
3. L. Selberg, "Radius measurement by interferometry," Opt. Eng. **31**, 1961–1966 (1992).
4. T. Schmitz, C. J. Evans, and A. Davies, "An investigation of uncertainties limiting radius measurement performance," in *Proceedings of ASPE Spring Topical Meeting* (American Society of Precision Engineering, 2000), p. 27.
5. T. Schmitz, A. Davies, and C. J. Evans, "Uncertainties in interferometric measurements of radius of curvature," Proc. SPIE **4451**, 432–447 (2001).
6. T. Schmitz, C. Evans, A. Davies, A., and W. T. Estler, "Displacement uncertainty in interferometric radius measurements," Ann. CIRP **51** (1), 451–454 (2002).
7. U. Griesmann, J. Soons, and Q. Wang, "Measuring form and radius of spheres with interferometry," Ann. CIRP **53**, 451–454 (2004).
8. A. Davies and T. Schmitz, "Defining the measurand in radius of curvature measurements," in *Proceedings of the SPIE 48th Annual International Symposium on Optical Science and Technology*, J. Decker and N. Brown, eds. (SPIE, 2003).
9. T. Schmitz, N. Gardner, M. Vaughn, and A. Davies, "Radius case study: optical bench measurement and uncertainty including stage error motions, in *Proceedings of the SPIE 50th Annual International Symposium on Optics and Photonics*, J. Decker and N. Brown, eds. (SPIE, 2005).
10. A. Davies and T. Schmitz, "Correcting for stage error motions in radius measurements," Appl. Opt. **44**, 5884–5893 (2005).
11. J. Denavit and R. Hartenberg, "A kinematic notation for lower-pair mechanisms based on matrices," J. Appl. Mech. **22**, 215–221 (1955).
12. R. Paul, *Robot Manipulators: Mathematics, Programming, and Control* (MIT Press, 1981).
13. A. Slocum, *Precision Machine Design* (Prentice-Hall, 1992).
14. P. Bevington and D. Robinson, *Data Reduction and Error Analysis for the Physical Sciences*, 2nd ed. (WCB/McGraw-Hill, 1992).
15. C. Evans, R. Hocken, and W. T. Estler, "Self-calibration: reversal, redundancy, error separation, and absolute testing," Ann. CIRP **45**, 617–634 (1996).
16. B. Taylor and C. Kuyatt, "Guidelines for evaluating and expressing the uncertainty of NIST measurement results," NIST Tech. Note 1297 (NIST, 1994).